Stability of an Idealized Floating Carpet of Plastic Spheres in an Open Channel Flow

Yan Toe, Chit; Uijttewaal, Wim; Wüthrich, Davide

DOI
10.1061/JHEND8.HYENG-1423

Publication date
2025

Document Version
Final published version

Published in
Journal of Hydraulic Engineering

ASCE

Stability of an Idealized Floating Carpet of Plastic Spheres in an Open Channel Flow

Chit Yan Toe[1]; Wim Uijttewaal[2]; and Davide Wüthrich[3]

Abstract: Plastic debris can accumulate at hydraulic structures and waste-collection devices, leading to a so-called *floating carpet* formation. Understanding the accumulation of plastic debris at structures is pivotal in the prediction of increased flood risk and design of waste-collection devices. In this research, we studied the stability of plastic carpets under different flow conditions using laboratory experiments, and we developed analytical models to predict critical velocities that led to two instabilities: (1) squeezing—particles inside the carpet are pushed downward due to cumulative compressive force, and (2) erosion—particles at the upstream edge of the carpet mobilize completely. Velocities of the fully developed flow were measured under a stable carpet to estimate boundary shear stress, which was applied to calculate the compressive force of the particles. Using measured flow velocity data and particle's properties, the critical flow velocities that led to instabilities were calculated. Overall, this research supports a better understanding of physical processes associated with plastic accumulation, supporting the development of optimized plastic removal strategies. **DOI: 10.1061/JHEND8.HYENG-14233.** © *2025 American Society of Civil Engineers.*

Practical Applications: This research investigates physical processes associated with waste accumulation or floating carpet at hydraulic structures such as flood gates, culverts, and waste-collection devices, using laboratory experiments and analytical considerations. In this study, we identified two kinds of carpet instabilities—squeezing and erosion. Two analytical formulas were derived for these two instabilities to estimate the critical flow velocity. Moreover, the amount of the collected waste can be anticipated for a given flow velocity by using these analytical formulas. Our research findings can underpin the design phase of collection devices and the choice of their deployment location.

Introduction

Plastic debris of different sizes, shapes, densities, and polymer compositions is constantly found in riverine, estuarine and marine environments, worsening their ecological and aesthetic values (Derraik 2002). Moreover, high volumes of plastic waste can increase the risk of urban flooding (Honingh et al. 2020), since accumulation of waste upstream of hydraulic structures (e.g., culverts, gates) reduces flow capacity of drainage systems (Ronckers et al. 2024). Therefore, removal and disposal of plastic debris from aquatic environments is an urgent issue, aligning with the United Nations' sustainable development goal number 14—*Conserve and sustainably use the oceans, seas and marine resources*.

Plastic debris in the ocean can be reduced in a cost-effective way if they are intercepted on land, since rivers are the main conveyors of debris toward the ocean (Meijer et al. 2021). Effective cleanup of plastic debris necessitates a thorough knowledge of not only their transport mechanisms in river systems, but also the impact of hydraulic structures on their pathways (Meijer et al. 2021). In fact, hydraulic structures including waste-collection devices disturb the transport of buoyant plastic debris in open channel flows, causing accumulation of debris upstream of the structures. This results in the formation of a so-called *floating carpet* (Fig. 1). Understanding the failure mechanism and stability criteria of the carpet is important for a better design of waste collection devices.

Similar accumulations of different materials is observed in rivers, for example, ice-jams (Guo et al. 2017; Parthasarathy and Muste 1994; Jueyi et al. 2010; Peters et al. 2017), and log-wood clogging at racks (Schalko et al. 2019), bridges (Burghardt et al. 2024), and flexible barriers (Piton et al. 2023). Most studies emphasize the impact of these accumulations on the increase of upstream water level. Among them, Jueyi et al. (2010) focused on the stability of a carpet composed of ice particles using laboratory experiments. They used a floating foam panel to simulate an ice-jam and considered the motion of floating particles as representative of ice particles. The same study developed a relationship between shear Reynolds number and dimensionless shear stress for the incipient motion of individual ice particles, the so-called Shields parameter. This parameter can be used to estimate flow velocity required for ice particles to move from their initial position.

Similarly, designing waste-collection devices requires a better understanding of carpet formation processes and carpet stability to effectively capture plastic debris. However, few studies have thoroughly investigated how plastic debris accumulates upstream of structures to form a carpet, and how this becomes unstable. Therefore, this study aims to better understand instability mechanisms of a floating carpet composed of buoyant spherical particles, including an assessment of the forces acting on it. An analytical framework is also developed to predict the threshold flow velocity for the particles to become unstable.

In this research, we idealized a buoyant carpet upstream of a hydraulic structure as shown in Fig. 2. Real plastic debris was simplified as spherical particles to focus on the fundamental physical processes of the carpet. A carpet is considered stable if particles'

[1]Ph.D. Candidate, Dept. of Hydraulic Engineering, Delft Univ. of Technology, Delft 2628CN, Netherlands (corresponding author). ORCID: https://orcid.org/0000-0003-1290-8115. Email: c.yantoe-1@tudelft.nl

[2]Professor, Dept. of Hydraulic Engineering, Delft Univ. of Technology, Delft 2628CN, Netherlands.

[3]Assistant Professor, Dept. of Hydraulic Engineering, Delft Univ. of Technology, Delft 2628CN, Netherlands. ORCID: https://orcid.org/0000-0003-1974-3560

Note. This manuscript was submitted on June 13, 2024; approved on December 13, 2024; published online on March 24, 2025. Discussion period open until August 24, 2025; separate discussions must be submitted for individual papers. This paper is part of the ***Journal of Hydraulic Engineering***, © ASCE, ISSN 0733-9429.

Fig. 1. Accumulation of plastic debris at waste-collection devices, creating the so-called *carpet*: (a) plastic debris captured by the floating boom, looking at upstream direction; and (b) aerial view of the carpet formations upstream of the waste-collection device. (Images courtesy of The Ocean Cleanup.)

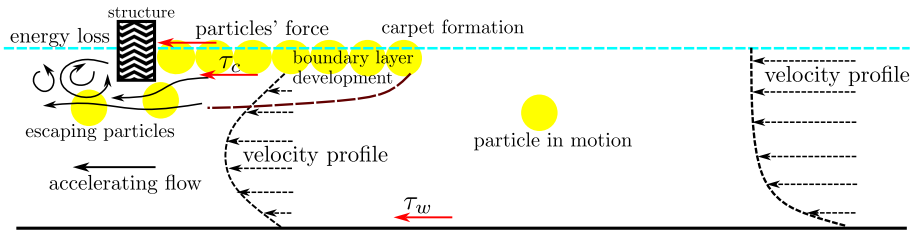

Fig. 2. Idealization of the carpet formation with buoyant spherical particles captured at a hydraulic structure. τ_c denotes the boundary shear stress under the carpet and τ_w the boundary shear stress at the bottom of the channel.

restoring forces (e.g., buoyancy) are in equilibrium with hydraulic forces (e.g., drag force). Otherwise, the carpet becomes unstable and consequently particles inside the carpet will move in flow direction (Jueyi et al. 2010). If a stable carpet is formed upstream of a hydraulic structure, a boundary layer develops under the carpet. Therefore, the velocity profile will transition from open channel flow to closed channel flow. Due to the carpet's additional resistance to the flow, upstream water level will also increase (Schalko et al. 2019).

This paper focuses on the incipient motion of buoyant spherical particles of a carpet through laboratory experiments in a hydraulic flume using different flow velocities, leading to the development of analytical formulas. This paper is organized as follows—the next section presents the conceptual models for stability of the carpet formation, the "Methods" section explains laboratory setups of the experiments conducted to investigate carpet stability and measure flow properties, the "Results and Discussion" section discusses experimental findings and implications for carpet stability, while the main conclusions are drawn in the final section.

Conceptual Model for Carpet Stability

In this section, a conceptual model [Fig. 3(a)] is developed for the stability of the carpet, considering forces acting on individual particles. The model is based on the Newton's second law that is the force balance acting on the particles. It is assumed that the hydraulic structure and individual particles do not deform due to the cumulative compressive force F_c of the particles and normal contact force F_n between particles. In a stable carpet, the forces acting on the particles are in equilibrium. This means that the buoyant force F_b and friction force F_t between particles balance the gravity force F_g in the vertical direction. Horizontally, the fluid drag force acting on the particle F_D is balanced by the reaction force F_n of the neighboring particle. The drag force is a hydrodynamic force that acts on the particles within the carpet in the flow direction. When particles are not perfectly aligned horizontally, the normal forces generate a vertical (destabilizing) component that could exceed the restoring buoyant force. This process is similar to the buckling phenomenon with compressed slender rods. In fact, Winkelmann et al. (2019) and Tordesillas and Muthuswamy (2009) observed buckling behavior for a line of spheres under a longitudinal compressive force and a restoring centripetal force. The linear chain of spheres can turn into a zig-zag pattern due to the longitudinal compressive force $(F_c + F_D)$ shown in Figs. 3(a and b) (Winkelmann et al. 2019). Kuhn and Chang (2006) and Tordesillas and Muthuswamy (2009) investigated theoretically and numerically the buckling phenomenon of a hexagonal close packing of the spheres to predict the positions of the particles in a matrix. However, in the present study the force chains of the carpet are in the horizontal plane and simplified to one dimension, as shown in Fig. 3(a) for the later analysis.

In this study, two instabilities are identified—(1) squeezing; and (2) erosion. *Squeezing* instability is defined as the configuration of the carpet in which the particles are pushed toward each other by horizontal compressive forces $(F_n \cos\theta = F_c + F_D)$, resulting in a vertical displacement once the perfect alignment is disturbed. This in turn leads to vertical downward force, which is $F_n \sin\theta = (F_c + F_D)\tan\theta$. Fig. 3(b) illustrates the squeezing phenomenon and defines variables at play. A buoyant particle inside the carpet

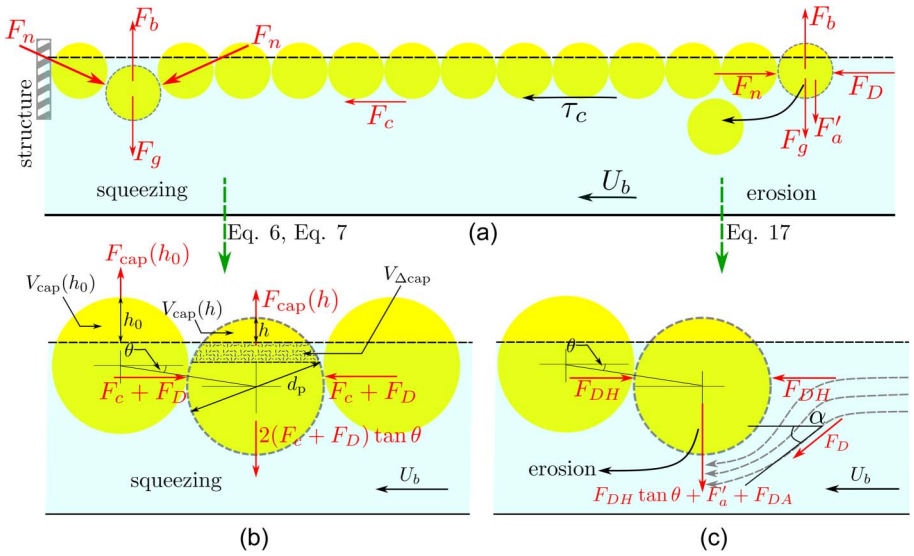

Fig. 3. Conceptual model for carpet stability: (a) overview of forces acting on the carpet; (b) squeezing instability due to unbalance between vertical component of the cumulative compression force and restoring force; and (c) erosion instability at the upstream edge owing to exceeding pressure fluctuation force and drag force. Normal force F_n is decomposed into horizontal component, $F_n \cos\theta = F_c + F_D$, and vertical component, $F_n \sin\theta = (F_c + F_D)\tan\theta$. In the figures, F_c denotes the compressive force, F_D the drag force on the particle, F_b the particle's buoyancy force, F_g the gravity force, F_a' the turbulent fluctuation force, F_{cap} the restoring force, F_{DH} horizontal component of F_D directing along the curved streamline, F_{DA} downward component of F_D resulting from the curved streamline, h_0 initial submerged height, V_{cap} emerged volume of the sphere, and θ the misalignment angle between the particles.

floats as long as its net buoyancy, later referred to as restoring force, is larger than downward destabilizing force. The potential restoring force is proportional to the emerged volume V_{cap} of the particle. Since the restoring force F_{cap} varies with the submerged volume and thus the vertical position of the sphere in water (or emerged height h of the sphere), we can write

$$F_{\text{cap}}(h) = \rho g V_{\text{cap}}(h) = \rho g \frac{\pi h^2}{3}\left(\frac{3}{2}d_{\text{p}} - h\right) \tag{1}$$

where

$$h = h_0 - d_{\text{p}} \sin\theta \tag{2}$$

in which h_0 = initial emerged height of the sphere before squeezing, g = acceleration due to gravity, d_{p} = diameter of the particle and θ = misalignment angle between the center of the squeezed sphere and the fully floating sphere [Fig. 3(b)]. Eq. (2) shows that (1) in the undisturbed situation $\theta = 0$ then $h = h_0$, and (2) once the particle gets gradually submerged, the condition $\theta > 0$ leads to $h < h_0$. Finally, for fully submerged spheres (i.e., $h = 0$), the maximum angle of submergence can be calculated as

$$\theta_{\max} = \arcsin\left(\frac{h_0}{d_{\text{p}}}\right) \tag{3}$$

and h_0 = found by solving for the volume equivalent to the reduced weight

$$\frac{\pi h_0^2}{3}\left(\frac{3}{2}d_{\text{p}} - h_0\right) = \left(1 - \frac{\rho_{\text{p}}}{\rho}\right)\frac{1}{6}\pi d_{\text{p}}^3 \tag{4}$$

where the left-hand side is the initial emerged volume $V_{\text{cap}}(h_0)$ that can be directly linked to the relative density of the particle, ρ_{p}/ρ where ρ_{p} is the density of the particle and ρ is the density of water.

During the squeezing process, the emerged volume of the sphere varies from the initially emerged volume $V_{\text{cap}}(h_0)$ to a smaller emerged volume $V_{\text{cap}}(h < h_0)$ by the amount of $V_{\text{cap}}(h_0) - V_{\text{cap}}(h)$ in which h goes from h_0 to 0. Therefore, the force required for this volume change $V_{\Delta\text{cap}}$ to sink in the water is

$$F_{\Delta\text{cap}}(h) = F_{\text{cap}}(h_0) - F_{\text{cap}}(h) = \rho g[V_{\text{cap}}(h_0) - V_{\text{cap}}(h)] \tag{5}$$

After some algebraic manipulations the required force $F_{\Delta\text{cap}}(h)$ can be expressed in terms of the misalignment angle θ as

$$F_{\Delta\text{cap}}(\theta) = \rho g \frac{\pi}{3}[3h_0 d_{\text{p}}^2(\sin\theta + \sin^2\theta) - 3h_0^2 d_{\text{p}} \sin\theta - d_{\text{p}}^3 \sin^2\theta(\sin\theta + 1.5)]$$

or

$$F_{\Delta\text{cap}}(\theta) = \underbrace{\rho g \frac{\pi}{6} d_{\text{p}}^3}_{\text{sphere weight}} \underbrace{\left[6\frac{h_0}{d_{\text{p}}}(\sin\theta + \sin^2\theta) - 6\frac{h_0^2}{d_{\text{p}}^2}\sin\theta - 2\sin^2\theta(\sin\theta + 1.5)\right]}_{\text{contribution due to changing geometry}} \tag{6}$$

Eq. (6) is shown in Fig. 4(a) as the dotted line depicting the relation between the generated restoring force $F_{\Delta\text{cap}}$ and the misalignment angle θ between two particles where the notation $\uparrow$ in the figure indicates that the force is pointing upward.

The vertical destabilizing force is acting on a particle within the carpet due to the vertical component of the cumulative compressive force transferred through the upstream particles. The cumulative compressive force consists mainly of (1) shear stress under the carpet F_c, and (2) drag force acting on the particle at the upstream edge of the carpet F_D. Only the vertical component of the cumulative compressive force $(F_c + F_D)$ will drag the sphere down by overcoming the required submerged force $F_{\Delta\text{cap}}(\theta)$. Therefore, for the sphere

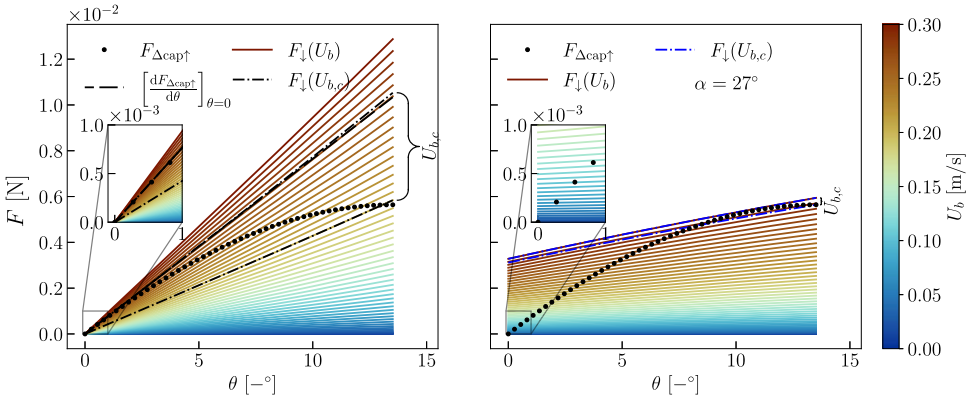

Fig. 4. Force balance between the required force for submergence $F_{\Delta\text{cap}\uparrow}$ [Eq. (6)] and downward force $F_{\downarrow}(U_b)$ [Eq. (10) for squeezing, and LHS of Eq. (17) for erosion]: (a) squeezing instability—Eq. (7); and (b) erosion instability—Eq. (15) at the angle of approach flow $\alpha = 27°$. The force balance around misalignment angle $\theta = 0$ are detailed in inset plots. In plot (a), the upper dash-dotted line represents the downward force for $U_{b,c} = 0.26$ m/s and the lower dash-dotted line for $U_{b,c} = 0.21$ m/s. Both figures are considered for sphere diameter $d_\text{p} = 20.0$ mm which is the large particle used in the experiments.

to be in equilibrium before squeezing occurs, there exists a vertical force balance such that

$$2(F_c + F_D)\tan\theta \le F_{\Delta\text{cap}}(\theta) \tag{7}$$

assuming that the tangential component of the friction between particles is negligible. It should be noted that since the particle is squeezed by the compressive forces from both sides [as shown in Fig. 3(b)], the left-hand side of Eq. (7) was multiplied by 2. The misalignment angle θ can initially be caused by the infinitesimal motion inherited from turbulent fluctuations or surface oscillations, and slight differences in densities of the particles within the carpet. This misalignment angle will generate the downward component of compressive force acting on the particle. If the stabilizing buoyant force is larger than the destabilizing force, then the particle will not move downward and the carpet can be considered as stable.

The contribution of the shear force F_c can be estimated by integrating the shear stress τ_c over the unit surface area of the carpet, which is product of the particle diameter d_p and carpet length λ, therefore resulting in $F_c = \tau_c \lambda d_\text{p}$. The shear stress acting on the carpet can be estimated as

$$\tau_c = \frac{1}{2}\rho C_f^\text{t} U_b^2 \tag{8}$$

where C_f^t = friction coefficient of the carpet and U_b = bulk flow velocity.

Next, the particle drag force F_D can be calculated as

$$F_D = \frac{1}{2}\rho C_D U_b^2 A_\text{p} \tag{9}$$

where C_D = drag coefficient of a sphere (≈ 0.5) and A_p = frontal area of the sphere, which is approximated (for simplicity) as its whole cross-sectional area, i.e., $A_\text{p} = \pi d_\text{p}^2/4$.

Therefore, the expression for the vertical component of the compressive force acting on the particle during squeezing process will be

$$2(F_c + F_D)\tan\theta = \underbrace{\frac{1}{2}C_D\rho U_b^2 \frac{\pi}{4}d_\text{p}^2}_{\text{particle drag force}} \underbrace{\left[\frac{8}{\pi}\frac{C_f^\text{t}}{C_D}\frac{\lambda}{d_\text{p}} + 2\right]}_{\text{carpet+edge}} \tan\theta \tag{10}$$

which defines the left-hand side (LHS) of Eq. (7). For the quantities used in the experimental work later on, Fig. 4(a) shows the relation of downward force and restoring force as a function of θ by substituting appropriate values for the parameters in Eqs. (6) and (10). To do so, we used the values $d_\text{p} = 20.0$ mm, $\rho_\text{p} = 861.7$ kg/m^3, $C_f^\text{t} = 10.88 \times 10^{-3}$, $\lambda = 2$ m, and $C_D = 0.5$ in the following analysis. It is noted that the maximum limit of the θ-axis in Fig. 4(a) shows that the particle will be fully submerged if the misalignment angle between the particles reaches the value of $\theta_\text{max} = 13.51°$ for a typical density ratio $\rho_\text{p}/\rho = 0.8617$.

The dotted line in Fig. 4(a) describes the required force for squeezing the particle, as described by Eq. (6), while the solid lines describe the downward force acting on the particle as mentioned in Eq. (10), both forces varying with θ. Again, the solid lines are represented for the downward force $F_{\downarrow}(U_b)$ for different bulk velocities U_b where the notation $\downarrow$ indicates downward direction. At $\theta \approx 0$, i.e. the condition with small misalignment or disturbance, high flow velocities are required for the particle to be dragged down, whereas the particles under larger disturbances (large θ) are more likely squeezed because of larger downward component of compressive force.

From Fig. 4(a), one can determine the flow velocity at which the particle is squeezed unconditionally, i.e., at $\theta = 0$, the so-called critical bulk velocity $U_{b,c}$ for squeezing instability. To find the critical velocity $U_{b,c}$, the slope of the buoyancy force $F_{\Delta\text{cap}}$ curve should be smaller than the slope of the downward force $F_{\downarrow}(U_b)$ curve near $\theta \approx 0$ in Fig. 4(a). Therefore, the critical bulk velocity that always results in instability is estimated by equating the slopes

$$U_{b,c} = \sqrt{\frac{\left[\frac{\mathrm{d}F_{\Delta\text{cap}}}{\mathrm{d}\theta}\right]_{\theta=0}}{C_D\rho\frac{\pi}{4}d_\text{p}^2\left(\frac{4}{\pi}\frac{C_f^\text{t}}{C_D}\frac{\lambda}{d_\text{p}} + 1\right)}} \tag{11}$$

where

$$\left[\frac{\mathrm{d}F_{\Delta\text{cap}}}{\mathrm{d}\theta}\right]_{\theta=0} = \rho g\frac{\pi}{6}d_\text{p}^3\left(6\frac{h_0}{d_\text{p}} - 6\frac{h_0^2}{d_\text{p}^2}\right) \tag{12}$$

as indicated by the dashed line. The corresponding downward force curve is also shown in Fig. 4(a) by the upper dash-dotted line that is very similar to the dashed line, especially near $\theta = 0$.

J. Hydraul. Eng., 2025, 151(4): 04025010

Contrary to such a strict definition of $U_{b,c}$ for unconditional squeezing regardless of the magnitude of the perturbation, there might be different definitions of $U_{b,c}$ for the particle to squeeze in case of strong perturbations. These circumstances can give rise to relatively low values of $U_{b,c}$ compared to the case of unconditional squeezing. Different values of $U_{b,c}$ for squeezing instability under different magnitudes of perturbations, i.e., from 0.21 m/s to 0.26 m/s, are indicated by the brace notation } in Fig. 4(a) while the lower limit of $U_{b,c}$ is denoted by the lower dash-dotted line and the upper limit is denoted by the upper dash-dotted line whose slope is $[\mathrm{d}F_{\Delta\mathrm{cap}}/\mathrm{d}\theta]_{\theta=0}$.

In case of total submergence, i.e., $\theta = \theta_{\max}$, the buoyant force $F_{\mathrm{cap}} = \pi/6(\rho_{\mathrm{p}} - \rho)gd_{\mathrm{p}}^3$ can be expressed in terms of the particle rise velocity u_s as follows:

$$F_{\mathrm{cap}} = \frac{1}{2}\rho u_s^2 C_D A_{\mathrm{p}} \tag{13}$$

And, since it is known that F_{cap} is balanced against the downward force defined in Eq. (10), we equate Eqs. (10) and (13) for the condition $\theta = \theta_{\max}$

$$\frac{1}{2}\rho u_s^2 C_D A_{\mathrm{p}} = \frac{1}{2}\rho U_b^2 C_D A_{\mathrm{p}}\left[\frac{8}{\pi}\frac{C_f^{\mathrm{t}}}{C_D}\frac{\lambda}{d_{\mathrm{p}}} + 2\right]\tan\theta_{\max} \tag{14a}$$

$$\frac{u_s^2}{U_b^2} = \left[\frac{8}{\pi}\frac{C_f^{\mathrm{t}}}{C_D}\frac{\lambda}{d_{\mathrm{p}}} + 2\right]\tan\theta_{\max} \tag{14b}$$

implying that ratio of rise velocity to bulk flow velocity at the onset of instability depends on the carpet length, drag, and friction coefficients.

In *erosion* instability, the particles upstream of the carpet are mobilized due to exceeding drag force compared to the restoring buoyancy force of the particle. Its graphical explanation is provided in Fig. 3(c). The erosion instability is expected to be independent of the carpet length because the particles at the upstream edge do not experience any compressive force from upstream. Regarding the erosion instability of the most-upstream particle, the driving force for the particle's movement is the combination of three forces indicated in Fig. 3(c). The first one is the downward component of the contact force induced by the adjacent particle, $F_{DH}\tan\theta$, in which F_{DH} denotes the horizontal component of the drag force directing along the curved streamline. The second one is turbulent (downward) fluctuation force F_a', and the third one is the downward component of drag force, F_{DA}, resulting from the streamline angle of the approach flow bending downward near the upstream edge of the carpet. Moreover, since the submergence of the particle can also increase the streamline angle, the total deflection angle of the streamline would be $(\alpha + \theta)$ in which α denotes the angle of the approach flow with respect to the horizontal axis.

Then, the force balance in vertical direction for erosion instability can be written as

$$F_{DH}\tan\theta + F_a' + F_{DA} \le F_{\Delta\mathrm{cap}}(\theta) \tag{15}$$

where

$$F_{DH} = \frac{1}{2}\rho C_D U_b^2 A_{\mathrm{p}}\cos(\alpha+\theta), \quad \text{and}$$
$$F_{DA} = \frac{1}{2}\rho C_D U_b^2 A_{\mathrm{p}}\sin(\alpha+\theta) \tag{16}$$

As for the definition of F_a', it can be considered as a pressure fluctuation multiplied by the submerged surface area of the sphere. Since the approach flow is fully developed it is expected that the large scale turbulence that reaches the free surface can induce a significant distortion of the particle's vertical position. According to Calmet and Magnaudet (2003), velocity fluctuations near the free surface can be characterized by the friction velocity u_*, implying that pressure fluctuations could also be characterized by $\rho u_*^2 = 0.5\rho C_f U_b^2$. Here, C_f denotes the friction coefficient of the flume bed as the turbulent fluctuations of the developed open channel flow are considered to be dominant.

Therefore, after rearrangements one can write Eq. (15) as

$$\frac{1}{2}\rho U_b^2 C_D A_{\mathrm{p}}\left[\cos(\alpha+\theta)\tan\theta + \frac{C_f}{C_D} + \sin(\alpha+\theta)\right] \le F_{\Delta\mathrm{cap}}(\theta) \tag{17}$$

Fig. 4(b) shows the relation between destabilizing force and restoring force of Eq. (15) for $\alpha = 27°$, which is the angle between vertical component and horizontal component of the approach flow measured in the laboratory experiment discussed in the "Methods" section and Appendix II. The parameters used in Fig. 4(b) are the same as in Fig. 4(a) and refer to a large particle with diameter $d_{\mathrm{p}} = 20.0$ mm.

As the erosion instability is defined by the condition of the leading edge particle that is completely detached from the neighboring particles, the force required for this instability to occur is equivalent to $F_{\Delta\mathrm{cap}}(h=0)$. When the particle is completely submerged, the required force does not change anymore, i.e., $\mathrm{d}F_{\Delta\mathrm{cap}}/\mathrm{d}\theta = 0$ but is equal to F_{cap}. Therefore in case of erosion instability $\theta = \theta_{\max}$, the required force F_{cap} [Eq. (13)] is balanced by the downward destabilizing force described in LHS of Eq. (17) as

$$\frac{1}{2}\rho u_s^2 C_D A_{\mathrm{p}} = \frac{1}{2}\rho U_b^2 C_D A_{\mathrm{p}}\left[\cos(\alpha+\theta_{\max})\tan\theta_{\max} + \frac{C_f}{C_D} + \sin(\alpha+\theta_{\max})\right] \tag{18a}$$

$$\frac{u_s^2}{U_b^2} = \cos(\alpha+\theta_{\max})\tan\theta_{\max} + \frac{C_f}{C_D} + \sin(\alpha+\theta_{\max}) \tag{18b}$$

Differently from the squeezing instability, here the ratio of particle's rise velocity to bulk velocity depends on the angle of approach flow α, but not on the carpet length, as expected.

To estimate the critical bulk velocity required for erosion instability, we equate F_{cap} with the driving force at the instance of total submergence $\theta_{\max}$, and after some mathematical manipulations we obtain

$$U_{b,c} = \sqrt{\frac{4(\rho-\rho_{\mathrm{p}})gd_{\mathrm{p}}}{3\rho C_D\left[\cos(\alpha+\theta_{\max})\tan\theta_{\max} + \frac{C_f}{C_D} + \sin(\alpha+\theta_{\max})\right]}} \tag{19}$$

The lower dash-dotted line in Fig. 4(b) shows the downward force of $U_{b,c}$ required for the complete submergence under strong perturbation which is predicted by Eq. (19). For the moderate and weak perturbations, however, we can also identify higher values of $U_{b,c}$ whose range is shown by the brace notation } in Fig. 4(b). The previously described phenomena will be used to interpret experimental observations.

Compared with the stability of ice particles, Jueyi et al. (2010) considered only the general incipient motion of the particles under a fixed floating foam panel. Contrarily, in our study the carpet instability was categorized into two mechanisms, depending on the specific location of the spheres within the floating carpet. This means

that the incipient motion considered by Jueyi et al. (2010) shows similarities with our definition of erosion instability, which depends on the flow velocity and particle properties, but not on the number of particles in the carpet. Therefore, this shared dependence is reflected in both mathematical expressions of Eq. (19) and the Shields criterion $\rho u_*^2/(gd_p(\rho-\rho_p))$ defined by Jueyi et al. (2010). However, since we emphasized the erosion of only the leading edge particles in the carpet, Eq. (19) considers the flow deflection angle α, which is not included in Jueyi et al.'s (2010) Shields criterion.

Methods

To validate the conceptual model, two different series of experiments were performed in the Hydraulic Engineering Laboratory of Delft University of Technology. The first series of experiments aimed at mapping the stability regime of the plastic carpet by measuring the flow discharge and water depth (to calculate flow velocity U_b) at the incipient motion of particles for different carpet lengths λ. The objective of the second series of experiments was to obtain the shear stress acting on the stable carpet formation by measuring the velocity profiles and consequently the cumulative compression force transferred by the upstream neighboring particles to the downstream particle of the carpet.

Dimensions of the flume are length = 14.30 m × width = 0.40 m × height = 0.40 m, as shown in Fig. 5. To simulate the gate, a wooden board was installed in the flume so that moving particles were captured at its upstream side causing a carpet formation, as shown in Fig. 5. The thickness of the hydraulic structure is 6 cm, its width is 40 cm (same dimension as flume width), and clearance between the bottom of the flume and the structure is 10 cm. Flow discharge was measured using Proline Prosonic Flow 91W ultrasonic flow meter, and water levels were measured using three Microsonic acoustic displacement meters (model—mic+35/IU/TC), located at 3.0 m and 1.0 m upstream and 1.0 m downstream of the hydraulic structure. The measured values were recorded digitally via DasyLab Data Acquisition System, allowing a good synchronization between all instruments.

Two different sizes of buoyant spherical particles were used to simulate the carpet formation of the plastic debris. For the bigger particle class, diameter of the particle is $d_p = 19.950$ mm $\pm$ 0.03% as measured by a vernier caliper device, and its mass was measured as 3.583 g $\pm$ 0.2% using the METTLER AT261 DeltaRange balance. Density of the particle was calculated by dividing its mass by the volume as $\rho_p = 861.7$ kg/m^3 $\pm$ 1%. For the smaller particle $d_p = 6.014$ mm $\pm$ 0.06% with a mass of 0.102 g $\pm$ 0.1%, its density is $\rho_p = 895.0$ kg/m^3 $\pm$ 1% using the same measurement procedure. For brevity, we will denote $d_p = 20.0$ mm and $d_p = 6.0$ mm for the big and small particles, respectively. The rise velocity of the particle, a property that shows the balance between buoyancy and drag forces, can be estimated by using an empirical formula based on the drag coefficient (White and Majdalani 2021). Particle's rise velocity reads

$$u_s = (\rho_p - \rho)g\sqrt{\frac{4d_p}{3\rho C_D}\frac{1}{|\rho_p - \rho|g}} \tag{20}$$

where C_D = drag coefficient of the particle computed as

$$C_D = \frac{24}{R_p} + \frac{6}{1+\sqrt{R_p}} + 0.4 \tag{21}$$

for a solid sphere at $R_p < 2 \times 10^5$ in which R_p = particle Reynolds number defined as $R_p \equiv u_s d_p/\nu$ where ν = kinematic viscosity (White and Majdalani 2021). Using iterative calculation, the rise velocity for the bigger particle was predicted as 0.273 m/s and 0.112 m/s for the smaller ones. In our experiment, theoretical values of rise velocity u_s of the particles were compared to experimental values measured using a 2 m high water column, detailed in Appendix I. After releasing the particle near the base of the water column, the particle's trajectory was recorded using a video recorder to calculate its rise velocity. This measurement was repeated for 13 times for bigger particles and 19 times for smaller particles. Different particles were used in each test to avoid any bias of manufacturing defects. The rise velocity of the bigger particle was found 0.211 $\pm$ 0.012 m/s and the rise velocity of the smaller one was 0.129 $\pm$ 0.006 m/s. The measured rise velocities are used in the subsequent analysis of carpet instability.

Experimental Setup for Experiments on Carpet Stability

This subsection describes the setup for the first series of experiments to investigate the stability of the carpet under different flow conditions. Therefore, for this experiment the motion of individual particles within the carpet was observed. Based on the analysis of carpet instabilities in the "Conceptual Model for Carpet Stability" section, it is expected that the squeezing instability is affected by the flow velocity and carpet length, normalized using the rise velocity

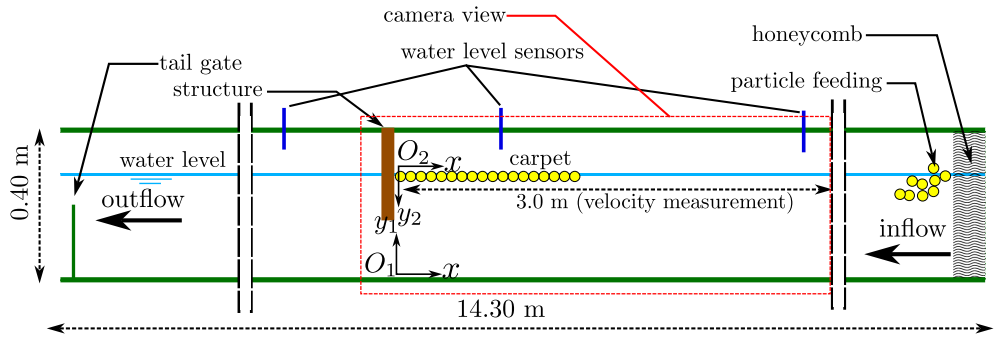

Fig. 5. Schematic representation of experimental setup for the carpet formation (not to scale). Velocity measurements were performed every 25 cm in a range of 3 m upstream of the structure. Two different coordinate systems were used to analyze velocity profiles: O_1 (from the bottom up) and O_2 (from the surface down).

J. Hydraul. Eng., 2025, 151(4): 04025010

and particle diameter, respectively, and the erosion instability is only by the flow velocity normalized by the rise velocity:

$$\underbrace{S = \mathcal{F}\left(\frac{\lambda}{d_p}, \frac{U_b}{u_s}\right)}_{\text{squeezing}} \quad \text{and} \quad \underbrace{S = \mathcal{F}\left(\frac{U_b}{u_s}\right)}_{\text{erosion}} \tag{22}$$

where S is a dimensionless Boolean value that gives True if the particle starts to move, or False if the particle remains its initial position.

Nine carpet lengths $\lambda/d_p \approx [25, 37.5, 50, 75, 87.5, 100, 125, 137.5, 150]$ using $d_p = 20.0$ mm, and six different lengths $\lambda/d_p \approx [50, 75, 100, 112, 125, 150]$ for $d_p = 6.0$ mm were analyzed for these experiments. During the tests, plastic particles were inserted in the flume near its upstream inlet and they developed a carpet of the required length under a constant low discharge (Fig. 5). With this discharge the water depth was 12 cm and with such a low discharge the particles accumulated at the hydraulic structure, creating a stable carpet. Then, the flow rate was gradually increased every 10 minutes. Since the tail gate in the flume was fixed during the experiments, the increase in discharge resulted in an increase in water level in the flume, which decreased the aspect ratio (i.e., flume width/water depth). Such a decrease can induce secondary currents in the flume, as discussed in Appendix II. The process of carpet formation and its changing configuration were captured using a video camera at 25 frames per second with 3,840×2,160 pixels resolution, and the camera view covered the complete length of each carpet as indicated in Fig. 5. The experiment was terminated the moment the particles in the carpet started to erode. Each test was repeated two times, with initial configuration of the carpet formation as similar as possible. Recorded videos were analyzed visually to observe the stability of the carpet. Once a particle inside the carpet layer became completely submerged, it was denoted as squeezing. Erosion was defined as the complete detachment of a particle from the upstream edge of the carpet. Bulk flow velocity U_b was calculated by dividing the measured discharge by the cross-sectional flow area (i.e., flume width times water depth) at the instances of squeezing and erosion for different carpet lengths. After determining the instability thresholds for squeezing and erosion, a second series of experiments was performed in the same flume to measure velocity profiles and turbulent characteristics, including Reynolds stress profiles in the stable flow regime, i.e., with flow velocity smaller than the critical velocity responsible for carpet instability.

Experimental Setup for Velocity Measurement under the Stable Carpet

In the second series of experiments, a stable carpet was generated based on the results of the first series. The flow discharge (Table 1) was kept constant throughout each experiment. To obtain information on the flow velocities and turbulence properties, detailed measurements were performed using two-dimensional laser Doppler velocimetry (LDV) system (WL-DelftHydraulics). The sensing volume of the LDV system is approximately 0.1 mm^3 and the laser intensity is 6 mW He-Ne with wavelength of 632.8 nm. The measuring principle of the current LDV system makes use of a reference beam combined with two Bragg-cell shifted signal beams to measure the Doppler shifts of the two components in the vertical plane (Rathakrishnan 2007). The length of the longest carpet examined in the experiment is 2 m and the shortest length is 0.5 m. All flow conditions are subcritical (F ≪ 1) and turbulent (R ≫ 8000). The velocity measurements with the particles of $d_p = 20.0$ mm are summarized in Table 1.

Table 1. Experimental flow conditions for velocity measurement using LDV system for the bigger particle $d_p = 20.0$ mm

Cases	H (cm)	Q ($\times 10^{-3}$ m^3/s)	λ (m)	R	F
Case 1	12	4.8	2.00	12,000	0.09
Case 2	12	4.8	1.00	12,000	0.09
Case 3	20	7.1	1.00	17,750	0.06
Case 4	11	3.4	0.75	8,250	0.07
Case 5	12	4.8	0.50	12,000	0.09

Note: H = water depth; Q = flow rate; R = Reynolds number ($= U_b H/\nu$); F = Froude number ($= U_b/\sqrt{gH}$); and U_b = bulk flow velocity.

Since the Froude number in this experiment (F ≈ 0.1, Table 1) is much smaller than the critical value F < 1, our experimental setup behaves similarly to the waste accumulation at hydraulic structures in the lowland rivers where the flow condition upstream of the structures is subcritical without noticeable free surface variation. This variation can affect the vertical motion of floating particles at the surface, influencing the stability of the carpet. More importantly, Reynolds number R in our experiment is sufficiently large to generate a turbulent flow despite higher R($\sim 10^6$) is often found in many rivers. Therefore, the friction coefficients and turbulence properties associated with the logarithmic velocity profile can be confidently applied in the analysis of the experimental data.

In each experiment, vertical profiles of horizontal and vertical flow velocities were measured every $x = 25$ cm from the upstream face of the hydraulic structure in the upstream direction, by moving the LDV horizontally on the rail of the flume and vertically with a traversing system. Since the goal was to obtain the flow properties very close to the carpet, the LDV device was installed upside down which implied that the flow could not be sampled closer than 5 mm from the bottom. To check consistency between velocity and discharge measurements, the measured velocity values of Case 4 were averaged over the water depth, and this depth-averaged velocity was compared to the discharge measurement of the acoustic flow meter. The difference was found to be 0.02×10^{-3} m^3/s, which is less than 1% and therefore considered acceptable.

Instantaneous horizontal and vertical components of the flow velocity were measured with a sampling frequency of 200 Hz to obtain vertical profiles of mean velocity and Reynolds stresses. The statistical independence of LDV measurement duration was checked by comparing the mean velocity and Reynolds shear stress for 2 min duration and 5 min duration. Since the comparison showed a good agreement between the data of two different sampling durations (Fig. S1 in Supplemental Materials), it was decided to conduct LDV measurements for 2 min. Measured profiles of Reynolds stresses can be used to estimate the friction velocity at the carpet and consequently its friction coefficient C_f^t to calculate the compressive force of the carpet F_c. Moreover, the friction velocity at the flume bottom can also be determined based on the Reynolds stress profile to estimate the turbulent fluctuation forces F_a' by means of ρu_*^2.

Results and Discussion

This section presents the results from the two series of experiments separately. The result of the first series describes the stability regime for the different lengths of carpet formation under various flow conditions. The second series discusses velocity profiles and turbulent properties under the stable carpet.

Stability Regime of the Carpet Formation

As shown in Eq. (22), the stability of the carpet depends on two dimensionless parameters—λ/d_p which indicates the number of

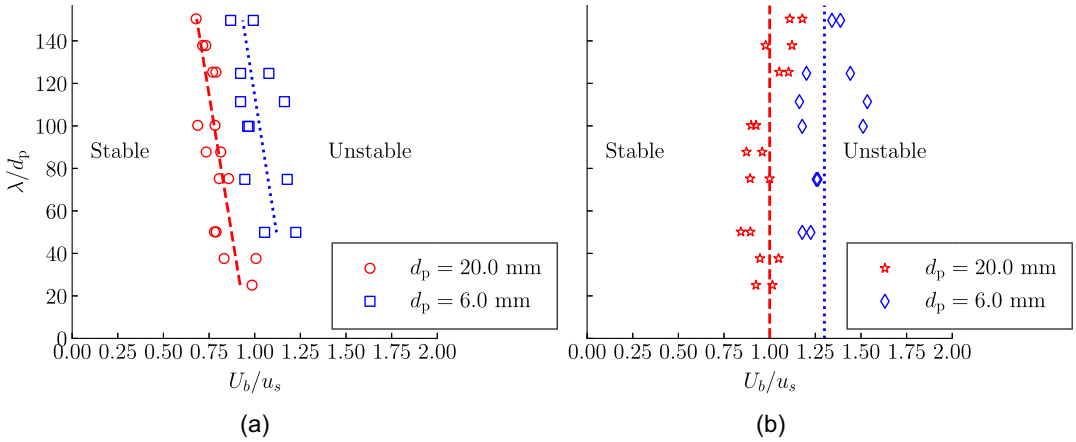

Fig. 6. Stability regimes of the carpet formation based on U_b/u_s and λ/d_p: (a) squeezing instability; and (b) erosion instability. Lines represent best-fit of the experimental data.

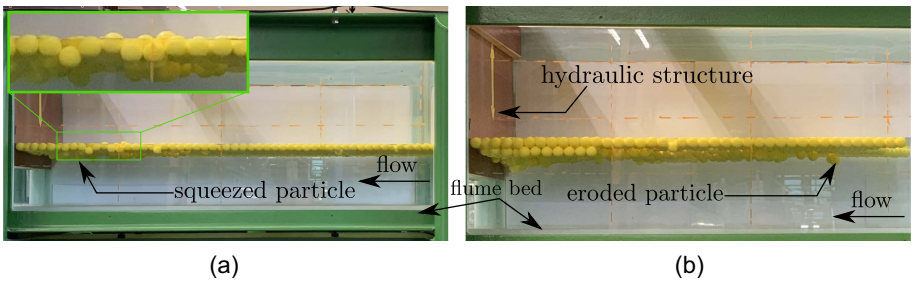

Fig. 7. Pictures of two instability modes of the carpet formation: (a) particles in the carpet are pushed against each other because of excessive force of the particles located in the upstream part of the carpet and hydrodynamic forces. Zig-zag pattern shown in inset is observed as a squeezing instability; and (b) once the flow rate reached a certain threshold, particles start to move from their initial location at the upstream edge to another location to form a multilayer formation. (a) Squeezing instability; and (b) erosion instability.

particles in a carpet length, and U_b/u_s which reflects the ratio of the fluid force to buoyant force of the particle. Based on these parameters, observations of the carpet stability are summarized in Fig. 6 for different carpet lengths and two particle sizes, $d_p = 20.0$ mm and $d_p = 6.0$ mm.

A stable carpet was observed when the average flow velocity U_b was smaller than the particle's rise velocity (Fig. 6). Once the flow velocity exceeded this threshold value, the carpet became unstable via two instability modes, squeezing and erosion, as explained in "Conceptual Model for Carpet Stability" section, and visualized in Figs. 7(a and b). In the experiments with longer carpets, squeezing instability occurred at lower velocities than erosion, whereas with short carpets both instabilities occurred with approximately the same velocity. When the erosion instability was triggered by flow velocity, the carpet configuration gradually transformed from a single-layer to a multilayer [Fig. 7(b)]. Similar observation of changes in carpet layers was also observed in the experimental study of debris jam studied by Zhang et al. (2024) although they used seedling trees to represent the debris. These cases were not considered in the present study.

The best-fit lines for each instability mode are shown in Fig. 6, although data points show some scatter most likely due to experimental disturbances by turbulence and surface waves, as well as imperfections in the carpet formation. Squeezing instability as observed in this experiment [Fig. 7(a)] is similar to the concept of buckling of linear force-chains in the research field of granular mechanics (Winkelmann et al. 2019; Tordesillas and Muthuswamy 2009).

Regarding erosion instability, we considered movement of the particles located *only* at the leading edge of the carpet [Fig. 7(b)]. Fitting lines of this instability are also shown in Fig. 6(b) for both experiments with $d_p = 20.0$ mm and $d_p = 6.0$ mm. A good agreement with vertical lines aligns with the theoretical analysis that predicts no dependency on carpet length.

However, the fitting lines for different particle sizes do not collapse on a single line in the nondimensional plot (Fig. 6). In particular, the stability of the smaller particles could be affected by forces not accounted for, e.g., surface tension. Moreover, secondary current in the flume explained in Appendix II can attribute to this discrepancy of erosion instability. Another observation concerns the unexpected flow pattern upstream of the carpet, where a weak upstream influence of the carpet on the flow at the free-surface was observed during the experiment. Due to these disturbances, the particles at the upstream edge of the carpet might not experience the full flow velocity (also shown in Appendix II), complicating the criterion of erosion instability. This unexpected flow behavior requires further study in dedicated experiments.

Flow Properties under a Stable Carpet

This section estimates the shear stress developed under the stable carpet by analyzing the velocity measurements under the longest carpet (Case 1 in Table 1). Two different coordinate systems were used to analyze the measured velocity profiles of Case 1 (Fig. 5). Lower coordinate system with origin O_1 at the bed with y_1 pointing

J. Hydraul. Eng., 2025, 151(4): 04025010

upward was applied for the study of flow near the bottom of the flume, whereas opposite-vertical coordinate system xO_2y_2 with the origin at the free surface was used to characterize the flow just below the carpet formation (Fig. 5).

Flow Development under a Stable Carpet

Qualitatively velocity data under the carpet showed an increasing velocity near the bottom and a decreasing velocity toward the free surface with a maximum value around the middle of the water depth [Fig. 9(b)]. For this reason it was decided to split the data into two parts for further analysis. To investigate the flow near the bottom of the flume and just below the carpet separately, the measured velocity profiles were divided based on the location of maximum flow velocity. The mean velocity profiles, $U(y_1)$ and $U(y_2)$, were fitted with the logarithmic laws of the wall [Eqs. (23) and (24)] by using their corresponding length scales for each part of the profile, respectively. To characterize the flow near the smooth bottom of the flume, the viscous length scale was used. Alternatively, a roughness length scale was used to normalize the vertical coordinate of Eq. (24), considering the carpet as a hydraulically rough wall.

Equation of the logarithmic profile for a smooth wall reads

$$U_1^+ = \frac{1}{\kappa}\ln y_1^+ + A \tag{23}$$

where $U_1^+ = U/u_{*\mathrm{b}}$, $y_1^+ = y_1 u_{*\mathrm{b}}/\nu$, $u_{*\mathrm{b}}$ = friction velocity at the bottom, κ = Von Kármán constant (= 0.412), A = integration constant which is a fitting parameter usually found approximately between 3.45 and 5.5.

For the hydraulically rough wall, the equation for the log-law of the wall reads

$$U_2^+ = \frac{1}{\kappa}\ln\frac{y_2 - y_0}{k} + B \tag{24}$$

where $U_2^+ = U/u_{*\mathrm{t}}$, $u_{*\mathrm{t}}$ = friction velocity at the top, y_2 is vertical direction of the opposite-vertical coordinate system xO_2y_2, y_0 is displacement height, k is roughness height, and B is an integration constant (Jackson 1981). It should be noted that analytical determination of y_0 for a rough boundary is an ongoing research in the community of fundamental fluid mechanics (Chung et al. 2021).

Figs. 8(a and b) present velocity profiles that show the development of the boundary layer in the downstream direction, toward the hydraulic structure. In Fig. 8(a), the measured velocity profiles were fitted by using Eq. (23) and lower coordinate system xO_1y_1, to characterize the flow at the bottom of the flume. The fitted logarithmic profile [Eq. (23)] is indicated by the linear black line in the semilogarithmic plot [Fig. 8(a)], proving that the lower part of the velocity profiles follows the classical logarithmic law of the smooth wall.

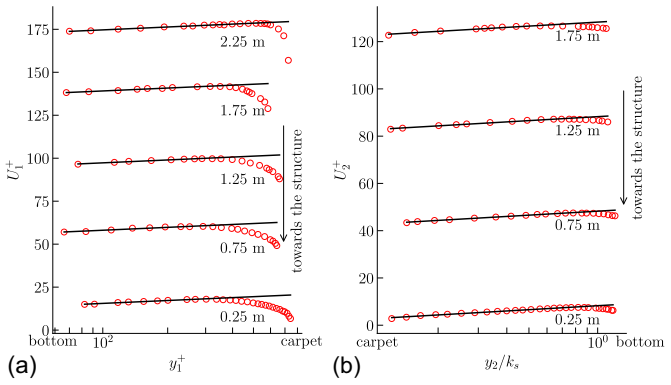

Fig. 8. Complete velocity profiles in semilogarithmic scale for Case 1 in Table 1: (a) velocity profiles near the bottom of the flume show a logarithmic profile after scaling with viscous length scale; and (b) velocity profiles beneath the carpet show a logarithmic profile by scaling with roughness length scale. In both plots, the velocity profiles are shifted by $\Delta U_1^+ = \Delta U_2^+ = 40$ for clear visualization: (a) smooth bottom wall; and (b) rough carpet.

Analysis of the velocity profiles starts with the most upstream section and ends toward the hydraulic structure through the carpet section, to describe the lower and upper parts of the profiles sequentially. At 2.25 m upstream of the hydraulic structure, the complete velocity profile follows the log-law of the wall, except near the free surface [Fig. 8(a)]. This deviation from the logarithmic law at the free surface is not easily explained. As mentioned earlier, the slight deviation of the mean velocity profile is likely affected by the influence of the carpet near the upstream free surface. Detailed investigation of this subtle phenomenon is yet to be carried out in future research.

At the leading edge of the carpet, i.e., 2 m upstream from the hydraulic structure, the velocity profile near the bed shows a logarithmic part although the integration constant is much larger than in the open channel flow cases. The obvious reason is because the flow is abruptly subjected to a change in boundary condition, i.e., a no slip upper boundary. As soon as the velocity profiles become developed toward the end of the carpet, i.e., 0.25 m and 0.5 m away from the hydraulic structure, the integration constants were found to be $A = 3.5$ and $A = 4.8$, respectively, implying the smooth bottom of the flume. Nevertheless, all the velocities follow logarithmic profiles [Eq. (23)] near the bottom of the flume. For the velocity profiles underneath the carpet, the upper part of the profile was considered separated by the location of maximum velocity and used the opposite-vertical coordinate system xO_2y_2 to analyze the development of the logarithmic profile.

Fully Developed Flow under a Stable Carpet

This section will assess whether the flow under the carpet attains fully developed condition, or not. For the fully developed flow in a closed or open channel, total shear stress varies linearly over the water depth according to

$$\frac{\tau_t}{\rho} \equiv -\overline{u'v'} + \nu\frac{\partial U}{\partial y} = u_*^2\left(1 - \frac{y}{H}\right) \tag{25}$$

where τ_t is the total shear stress and $-\rho\overline{u'v'}$ the Reynolds stress (Nieuwstadt et al. 2016). The experimental profiles of the Reynolds stresses changed gradually from the fully developed open channel flow upstream of the carpet (3 m upstream from the hydraulic structure) to the developed closed channel condition at the innermost region of the carpet (0.25 m upstream from the hydraulic structure) in Case 1 [Fig. 9(a)]. This indicates that the flow is transitioning from developed open channel flow to developed closed channel flow through the development of a boundary layer under the carpet. For both developed flows, the Reynolds stress profile showed a linear relation with the water depth, dictated by Eq. (25). Between these two locations, the stress profiles depicted a nonlinear trend near the upper part of the water depth, typical of the transition region. Fig. 9(b) shows the velocity profile and Reynolds shear stress profile measured at 0.25 m upstream of the hydraulic structure, the location with the most developed flow. Data show that the location of zero Reynolds shear stress $-\rho\overline{u'v'} = 0$ is slightly different from the location of maximum flow velocity $U_{\max}$, and is found slightly closer to the smooth wall than the location of $U_{\max}$. This is in agreement with experimental observations of (Tatinclaux and Gogus 1983; Hanjalić and Launder 1972) who studied asymmetric plane flows between smooth and rough walls.

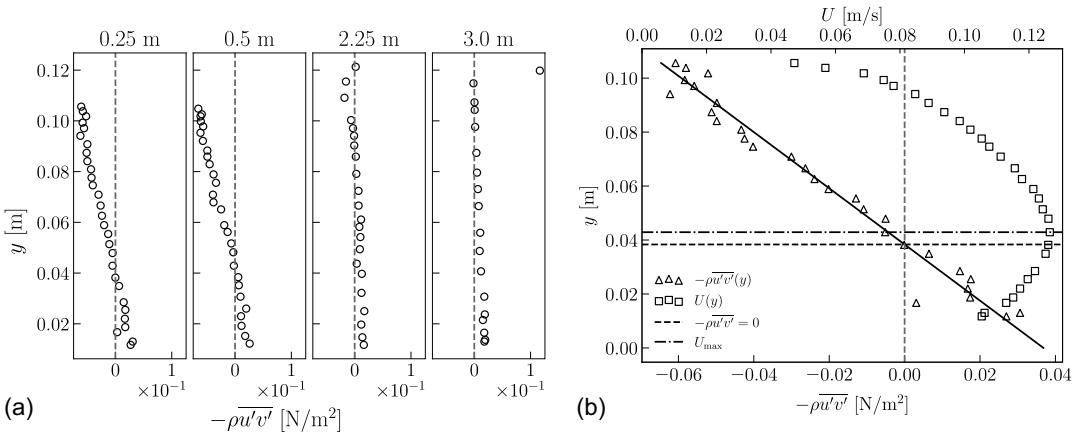

Fig. 9. Velocity and turbulent properties measured under a 2 m stable carpet: (a) measured Reynolds stress profiles between 3.0 m and 0.25 m upstream from the structure; and (b) measured velocity and Reynolds stress profiles at 0.25 m location. Position of $-\rho\overline{u'v'} = 0$ is slightly closer to the smooth wall than the position of $U_{\max}$.

Even though it was shown in Fig. 8(b) that the velocity profiles underneath the carpet obey the logarithmic law [Eq. (24)] qualitatively, the fitting procedure to the measured velocity profile needs to be discussed. One way to obtain u_{*t} is through fitting the measured velocity data with the log-law of the wall for the inner layer [Eq. (24)]. A second method is via fitting the measured Reynolds stress profile to a linear function [Eq. (25)], as shown by the straight line in Fig. 9(b). Using this linear-fit profile, the friction velocities at the carpet and at the bed can be extrapolated. For consistency, these methods should provide similar values for both friction velocities u_{*t} and u_{*b}. After application of an iterative procedure to optimize the fit with Eq. (24), a virtual shift $y_0 = 0.86$ cm and a best-fitting value $\kappa = 0.35$ are obtained for roughness height $k = 1$ cm (which is the radius of the sphere). Such a change in κ value was previously reported by Breugem et al. (2006) for a flow over a porous surface, which is similar to our case.

Regarding the virtual shift $y_0 = 0.86$ cm, this was measured from the water surface, or $y_0 = 0.674$ cm if measured from the bottom of the sphere. Measuring y_0 from the bottom of the sphere in our floating carpet makes fair comparison of y_0/D with the literature which measured y_0 from the top of the particle in sediment transport research. In this study, we obtained $y_0/D = 0.337$. In the literature, for example, Einstein and El-Samni (1949), Kironoto et al. (1994), and Afzalimehr and Rennie (2009), they measured y_0 from the top of the sphere toward the bed, and obtained approximately $y_0/D = 0.2$ and $y_0/D = 0.25$, confirming that our result $y_0/D = 0.337$ does not deviate much from these values.

The fitting procedure provides the friction velocity at the top $u_{*t} = 8.6 \times 10^{-3}$ m/s and an integration constant $B = 8.62$. The continuous black curve in Fig. 10 shows the resulting best-fitted profile. This best-fitted friction velocity $u_{*t} = 8.6 \times 10^{-3}$ m/s agrees with the $u_{*t} = 8.4 \times 10^{-3}$ m/s obtained by fitting the Reynolds stress profile. The latter values is therefore used for the analysis of carpet instabilities.

The velocity profile of the inner layer near the bottom was fitted with the log-law of the smooth wall [Eq. (23)]. The fitted velocity profile is indicated by the black dashed line in Fig. 10. The conventional value of $\kappa = 0.412$ was used. The friction velocity at the bottom, was found to be $u_{*b} = 7.38 \times 10^{-3}$ m/s with this method, while the method of fitting the Reynolds stress profile provided $u_{*b} = 6.07 \times 10^{-3}$ m/s. This discrepancy is considered acceptable given the limitations of the experimental approach, especially near the bottom. The value $u_{*b} = 6.07 \times 10^{-3}$ m/s is used for the analysis of instabilities explained later.

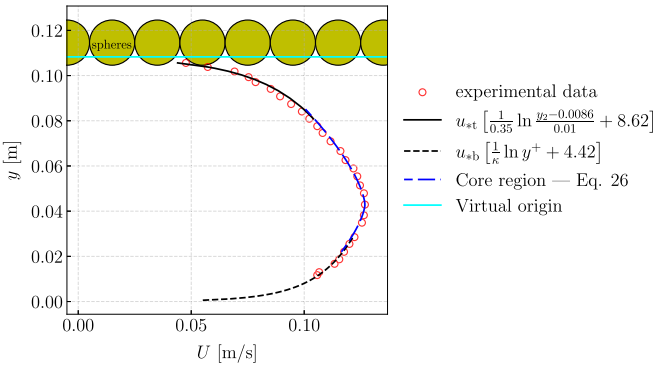

Fig. 10. Fitting velocity profile with log-laws of the wall. Eq. (23) is used for smooth bottom part, and Eq. (24) is used for the rough carpet part with $\kappa = 0.35$, $k = 1$ cm and $y_0 = 0.86$ cm. The central part of the profile is fitted using power law Eq. (26).

The central part of the velocity profile can be approximated by a power law considering each outer layer of the separate profiles as the core region, in line with Nieuwstadt et al. (2016). The power law of the velocity profile reads

$$U_i = U_{\max} - \frac{2}{3}\frac{u_{*i}}{\beta_i}\left(1 - \frac{y}{H_i}\right)^{1.5} \tag{26}$$

where the index variable i becomes b for the bottom case and t for the carpet case, β = experimental parameter (≈ 0.13), H_i = water depth for each ith part up to the location of $U_{\max}$. The fitted profiles for each outer part of the velocity profile are shown by the long dashed lines in Fig. 10, providing an excellent agreement with measured data with $\beta_b = 0.132$ and $\beta_t = 0.115$.

Analysis of the Stability of Floating Carpets

With the measurements of the flow properties, the squeezing and erosion instabilities of the carpets can now be further investigated using the analytical model developed in "Conceptual Model for Carpet Stability" section. In particular Eqs. (11) and (19) will be applied.

J. Hydraul. Eng., 2025, 151(4): 04025010

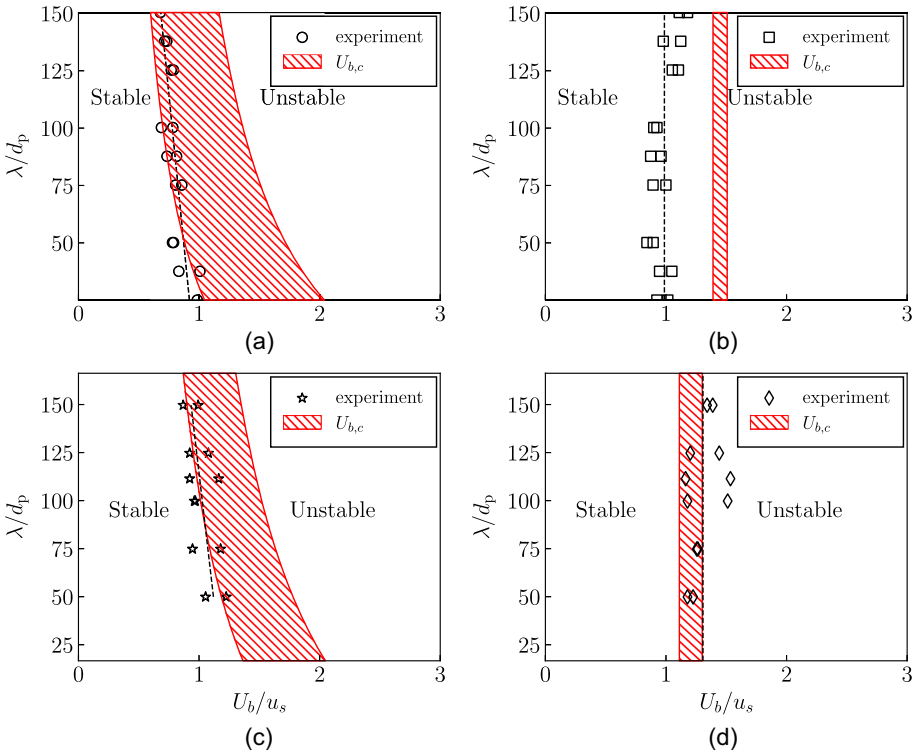

Fig. 11. Comparison between stability regimes defined by experimental results and analytical model for the particle of (a and b) $d_p = 20.0$ mm with $C_f^t = 11 \times 10^{-3}$; and (c and d) $d_p = 6.0$ mm with $C_f^t = 4.59 \times 10^{-3}$. Hatched regions indicate a range of theoretical predictions of $U_{b,c}$ for squeezing and erosion. U_b was normalized by $u_s \pm$ range, which is the variation of u_s among the particles.

The friction coefficient C_f needed for the theoretical model is the squared ratio of friction velocity u_* and bulk velocity U_b according to

$$C_f \equiv 2\left(\frac{u_*}{U_b}\right)^2 \tag{27}$$

using the bulk velocity U_b and the specific friction velocities u_* as found for the top and bottom, yielding $C_f^t = 11 \times 10^{-3}$ and $C_f^b = 6.2 \times 10^{-3}$ using the measured data of Case 1, the fully developed flow under a 2 m carpet.

In order to compare the analytical model with the experimental results for squeezing instability, upper and lower limits of $U_{b,c}$ were calculated for different carpet lengths. The resulting range of $U_{b,c}$ is shown in Figs. 11(a and c) by means of left-slanting hatch for $d_p = 20.0$ mm and $d_p = 6.0$ mm, respectively. In these figures, the bulk velocity was normalized with particle's rise velocity u_s, considering its variability among different particles. Analytical prediction shows good agreement with experimental finding for both cases of $d_p = 20.0$ mm and $d_p = 6.0$ mm within the measurement accuracy [Figs. 11(a and c)], confirming the validity of the theoretical model.

For erosion instability, the force due to turbulent pressure fluctuations F_a' in Eq. (15) was estimated using u_* obtained in the open channel section of the flume, not affected by the carpet. Fitting the measured Reynolds stress profile provided $u_* = 4.62 \times 10^{-3}$ m/s and $C_f = 6.2 \times 10^{-3}$ for the bottom of the flume. As discussed earlier, upper and lower limits of $U_{b,c}$ can be estimated using the analytical model. The range of resulting $U_{b,c}$ is shown in Figs. 11(b and d) with the left-slanting hatch showing variability in particle sizes, respectively. Apparently the analytical model for erosion instability is slightly over-predictive for the case of $d_p = 20.0$ mm showing that higher flow velocity is required for erosion than the experimental observation [Fig. 11(b)]. However, in case of $d_p = 6.0$ mm the predicted range of $U_{b,c}$ lies within the experimental results [Fig. 11(d)]. In both cases, variability of u_s was also considered when normalizing the bulk velocity.

Such a difference in prediction of critical flow velocity for squeezing and erosion can be traced back to (1) imprecise estimation of friction coefficients of the flume, (2) local effect of instantaneous turbulent fluctuations, (3) influence of free surface fluctuations, (4) secondary circulation in the flume as discussed in Appendix II, (5) uncertainties in measurement of the angle of approach flow α toward the carpet, and (6) variability of the particles. Moreover, the model might not properly consider the effect of the lift force resulting from the streamline curvature around the particle, that causes the particle to be more unstable. The prediction accuracy could benefit from a more detailed view on the flow around the upstream edge of the carpet, as well as the configuration of the particles inside the carpet. Further experiments are recommended in a longer flume with more space to allow for fully developed conditions both upstream and underneath the carpet.

Conclusions

Understanding the physical processes of plastic waste accumulation in the form of a floating carpet is important to better design waste collection devices and optimize hydraulic structures. This paper investigates the stability of the floating carpet using an analytical model based on physical considerations and laboratory experiments.

Accumulation of plastic particles upstream of hydraulic structures can become unstable via two instability mechanisms: (1) squeezing and (2) erosion. An analytical framework is proposed for these

instability mechanisms. Together, the analytical model and experimental data show that squeezing instability of the carpet depends on two dimensionless parameters: (1) λ/d_p which is the number of plastic particles, and (2) U_b/u_s which is a competition between downward and restoring forces. Erosion instability, however, depends only on the second parameter because the particles at the carpet edge do not experience cumulative compressive force. The carpet's roughness coefficient C_f^t is necessary to estimate threshold velocity $U_{b,c}$ of squeezing instability [Eq. (11)] via estimation of shear stress. The friction coefficient C_f^t is determined based on the particles' features including their diameter and carpet layout. The bottom friction coefficient of an open channel C_f and approach angle α are important parameters to estimate the critical bulk velocity $U_{b,c}$ of erosion instability [Eq. (19)]. C_f can be estimated based on the roughness features of the river bed. Determining the approach angle α requires two-dimensional velocity measurements close to the free surface near the upstream edge of the carpet. Variation of u_s due to particle's non-uniformity can also change threshold velocity of instabilities.

Moreover, measured velocity data shows that porosity of the carpet reduces Von Kármán constant from 0.412 to 0.35, which changes the slope of velocity profile near the carpet. Therefore, some care is needed to estimate shear stress of the carpet using the conventional logarithmic velocity profile. To elucidate flow structures at the leading edge and near the voids of the carpet, particle image velocimetry (PIV) measurements are recommended that capture spatial high-resolution of the flow. Moreover, compressive force of the carpet should be directly measured using force sensors to compare with indirect estimation of using Reynolds shear stress. Altogether these results provide a better understanding of physical mechanisms of waste accumulation at hydraulic structures. Besides, squeezing and erosion instabilities may be harnessed in certain types of hydraulic structures that extend further in the water to capture a larger amount of debris, avoiding a larger floating surface area in the open channel.

Appendix I. Measurement of Rise Velocity of Particles

The rise velocity of the particles were measured using a water column of 2 m length and 15 cm width, as shown in Fig. 12. To release the particle near the base of the water column, the particle was first inserted into the top opening of L-shaped pipe. Particle was pushed down through the pipe using a stick gradually until the particle reached to the bend of pipe. Once the particle passes the bend of the pipe, it exits the pipe instantly and rises due to its buoyancy.

The motion of the particle was recorded using a video camera. To measure the distance traveled by the particle, a ruler was attached on the water column so that the camera records the motion of the particle passed through 30 cm distance as shown in Fig. 12. This 30 cm distance is assumed for the particle to rise with terminal velocity, that is free from initial acceleration. Time taken for this distance, Δt, was also recorded and used to calculate the rise velocity of the particle according to

$$u_s = \frac{0.3[\text{m}]}{\Delta t[\text{s}]} \tag{28}$$

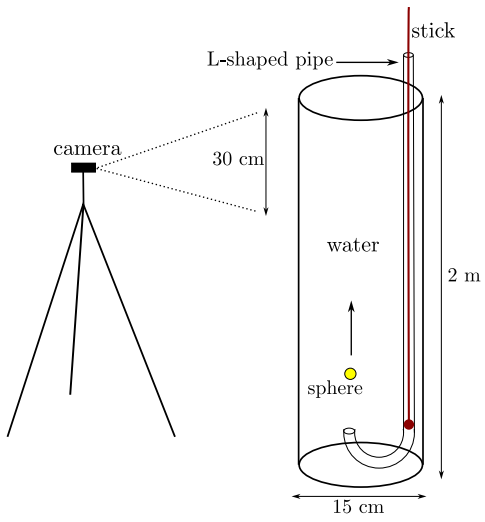

Fig. 12. Experiment set-up to measure rise velocity of the particles.

Appendix II. Analysis of Secondary Currents

Existence of secondary currents is assessed and quantified in this appendix for the open channel flow case without particles, and for the 2 m long carpet case. For the latter case, the approach flow angle α is estimated as well.

Secondary currents can be observed in a turbulent straight channel, especially when the aspect ratio (i.e., flume width/water depth) is smaller than 5, due to anisotropy in the Reynolds stresses (Nezu 2005). This secondary current induces the downward vertical velocity near the center line of the channel. Such a downward vertical velocity can enhance erosion instability of the particles at the upstream edge of the carpet. The existence of secondary currents was examined in the open channel flow with the hydraulic structure (Fig. 5 without the carpet). Fig. 13 shows the profiles of horizontal and vertical velocities at different measurement locations. The influence of the hydraulic structure is visible even 1.25 m upstream of the structure. The vertical velocity profile at 2.25 m (right in Fig. 13) shows a mean downward vertical velocity of approximately $0.06U_{\max}$.

Fig. 14 shows the profiles of horizontal and vertical velocity along the flume for the 2 m carpet case i.e., Case 1 in Table 1. At 3.0 m upstream of the hydraulic structure which is an open channel section (which is 1 m upstream of the carpet), vertical velocity of $U_y \approx 0.06U_{\max}$ was also found, implying the influence of secondary

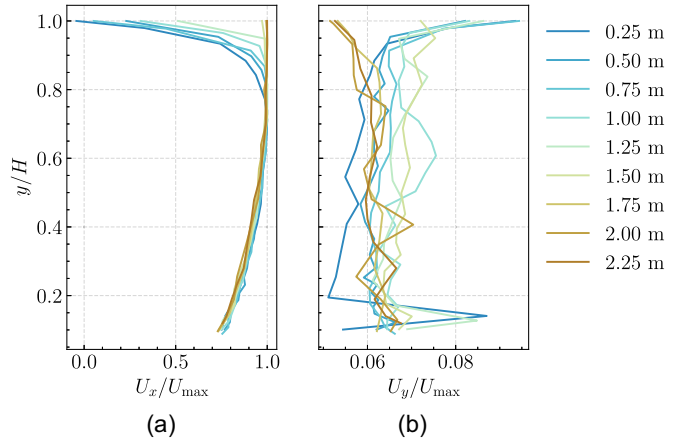

Fig. 13. Vertical profiles of (a) horizontal; and (b) vertical velocity components at different locations in the open channel flow without particles. The location of 0.25 m is the closet location to the hydraulic structure, confirming its influence on the velocity profiles.

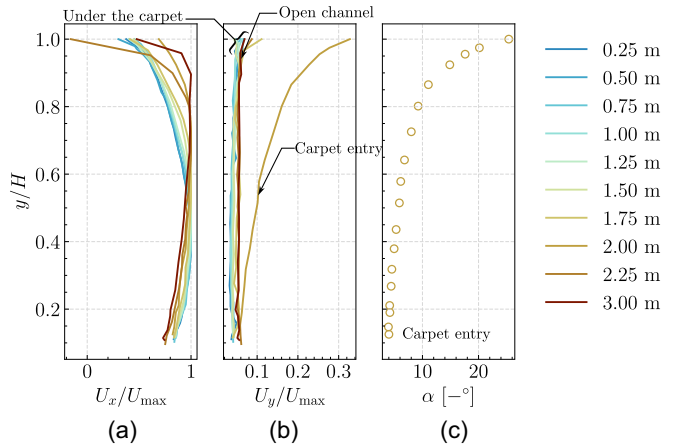

Fig. 14. Vertical profiles of (a) horizontal; and (b) vertical velocity at the open channel flow, at the carpet entry, and under the 2 m carpet. (c) Flow angle α along the water column at the carpet entry, $x = 2.00$ m. The angle represents the deflection of streamlines. The legends in the figure indicate the measurement distance upstream of the hydraulic structure.

currents on the erosion instability even for the case of aspect ratio of 3.3.

To estimate the angle of the approach flow near the upstream edge of the carpet, we applied the following relation to find the velocity angle in the vertical plane as

$$\alpha = \arctan\left(\frac{U_y}{U_x}\right) \tag{29}$$

where U_y and U_x = vertical and horizontal components of the flow velocity, respectively. Two-dimensional LDV measurements can provide U_y and U_x (of the fixed Cartesian coordinate system) along the water depth and consequently angle α of the velocity vector or streamline can be estimated using Eq. (29). Fig. 14 shows velocity components (U_x, U_y) and calculated flow angle α at 2.00 m upstream of the carpet which is the upstream edge of the 2 m carpet (Case 1 in Table 1).

In Fig. 14 the maximum deflection angle is found at the free surface, implying that the streamline bends down near the upstream edge of the carpet. The resulting information can be used in Eq. (19) to predict the erosion instability of the particle exposed to the bending streamlines.

Data Availability Statement

Velocity data obtained by LDV measurements are available from the corresponding author upon reasonable request.

Acknowledgments

This research project is funded by NUFFIC through the Orange Knowledge Programme, Rijkswaterstaat, and the seed funds of the Climate Action Programme at TUDelft. Antonio Magherini, a master student from the same university, is acknowledged for his contribution to the experimental work. We are grateful to Dr. Ton van den Bremer for generously lending the plastic spheres.

Notation

The following symbols are used in this paper:

A, B = integration constants in Eqs. (23) and (24);
A_p = frontal area of the sphere (m^2);
C_D = drag coefficient of the sphere;
C_f = friction coefficient of the flume bed in the open channel section;
C_f^b, C_f^t = friction coefficient at the bed in the carpet section, and at the carpet, respectively;
d_p = particle's diameter (m);
F = Froude number, $F = U_b/\sqrt{gH}$;
F_a' = turbulent fluctuation force (N);
F_b = buoyant force (N);
F_c = compressive force (N);
F_{cap} = restoring force (or) force required for V_{cap} to submerge (N);
$F_{\Delta cap}$ = force required for $V_{\Delta cap}$ to submerge in the water (N);
F_D = drag force (N);
F_{DA} = downward component of F_D resulting from the streamline angle of the approach flow (N);
F_{DH} = horizontal component of F_D directing along the curved streamline (N);
F_g = gravity force (N);
F_n = normal contact force (N);
F_t = friction force between particles (N);
g = acceleration due to gravity (m/s^2);
H = water depth (m);
h = emerged height of the sphere (m);
h_0 = initial emerged height of the sphere (m);
k = roughness height (m);
Q = discharge (m^3/s);
R = Reynolds number, $R = U_b H/\nu$;
R_p = particle Reynolds number, $R_p = u_s d_p/\nu$;
S = dimensionless Boolean value to determine stability;
$U(y)$ = mean velocity profile (m/s);
U_b = bulk flow velocity (m/s);
$U_{b,c}$ = critical bulk velocity of instabilities (m/s);
U_{max} = maximum velocity (m/s);
U_x, U_y = x- component, and y- component of U, respectively (m/s);
U_1^+, U_2^+ = mean velocity normalized by u_{*b} and u_{*t}, respectively;
u_s = particle rise velocity (m/s);
u_* = friction velocity (m/s);
u_{*b}, u_{*t} = friction velocity at the bed in the carpet section, and at the carpet, respectively (m/s);
V_{cap} = emerged volume of the sphere (m^3);
$V_{\Delta cap}$ = change in submerged volume of the sphere (m^3), $V_{\Delta cap} = V_{cap}(h_0) - V_{cap}(h)$;
x = horizontal axis (positive to the right);
y_0 = displacement height (m);
y_1 = vertical axis pointing upward from the flume bottom;
y_1^+ = y_1 normalized by viscous length scale;
y_2 = vertical axis pointing downward from the water surface;
y_2^+ = y_2 normalized by roughness length scale;
β = experimental parameter for Eq. (26);
λ = carpet length (m);
κ = Von Kármán constant;
θ = misalignment angle between the particles (rad);

θ_{max} = maximum angle of θ, or total submergence;
ρ_p = particle's density (kg/m^3);
ρ = water density (kg/m^3);
$-\rho\overline{u'v'}$ = Reynolds stress (N/m^2) where u' and v' are fluctuations of horizontal and vertical velocities;
τ_c = shear stress over the unit surface area of the carpet (N/m^2);
τ_t = total shear stress (N/m^2);
ν = kinematic viscosity (m^2/s); and
$\uparrow, \downarrow$ = upward and downward direction.

Supplemental Materials

Fig. S1 is available online in the ASCE Library (www.ascelibrary.org).

References

Afzalimehr, H., and C. D. Rennie. 2009. "Determination of bed shear stress in gravel-bed rivers using boundary-layer parameters." *Hydrol. Sci. J.* 54 (1): 147–159. https://doi.org/10.1623/hysj.54.1.147.

Breugem, W., B. Boersma, and R. Uittenbogaard. 2006. "The influence of wall permeability on turbulent channel flow." *J. Fluid Mech.* 562 (Sep): 35–72. https://doi.org/10.1017/S0022112006000887.

Burghardt, L., D. W. Poppema, L. Bénet, D. Wüthrich, S. Erpicum, and E.-M. Klopries. 2024. "Multi-lab investigation of the effect of debris composition on bridge clogging during floods." In *Proc., 10th Int. Symp. on Hydraulic Structures (ISHS 2024)*, 791–800. Zurich, Switzerland: ETH Zurich.

Calmet, I., and J. Magnaudet. 2003. "Statistical structure of high-Reynolds-number turbulence close to the free surface of an open-channel flow." *J. Fluid Mech.* 474 (Jan): 355–378. https://doi.org/10.1017/S0022112002002793.

Chung, D., N. Hutchins, M. P. Schultz, and K. A. Flack. 2021. "Predicting the drag of rough surfaces." *Annu. Rev. Fluid Mech.* 53 (1): 439–471. https://doi.org/10.1146/annurev-fluid-062520-115127.

Derraik, J. G. 2002. "The pollution of the marine environment by plastic debris: A review." *Mar. Pollut. Bull.* 44 (9): 842–852. https://doi.org/10.1016/S0025-326X(02)00220-5.

Einstein, H. A., and E.-S. A. El-Samni. 1949. "Hydrodynamic forces on a rough wall." *Rev. Mod. Phys.* 21 (3): 520. https://doi.org/10.1103/RevModPhys.21.520.

Guo, J., H. Shan, H. Xu, Y. Bai, and J. Zhang. 2017. "Exact solution for asymmetric turbulent channel flow with applications in ice-covered rivers." *J. Hydraul. Eng.* 143 (10): 04017041. https://doi.org/10.1061/(ASCE)HY.1943-7900.0001360.

Hanjalić, K., and B. Launder. 1972. "Fully developed asymmetric flow in a plane channel." *J. Fluid Mech.* 51 (2): 301–335. https://doi.org/10.1017/S0022112072001211.

Honingh, D., T. van Emmerik, W. Uijttewaal, H. Kardhana, O. Hoes, and N. van de Giesen. 2020. "Urban river water level increase through plastic waste accumulation at a rack structure." *Front. Earth Sci.* 8 (Feb): 1–8. https://doi.org/10.3389/feart.2020.00028.

Jackson, P. 1981. "On the displacement height in the logarithmic velocity profile." *J. Fluid Mech.* 111 (Oct): 15–25. https://doi.org/10.1017/S0022112081002279.

Jueyi, S., W. Jun, H. Yun, and K. Faye. 2010. "Velocity profiles and incipient motion of frazil particles under ice cover." *Int. J. Sediment Res.* 25 (1): 39–51. https://doi.org/10.1016/S1001-6279(10)60026-1.

Kironoto, B., W. H. Graf, and Reynolds. 1994. "Turbulence characteristics in rough uniform open-channel flow." *Proc. Inst. Civ. Eng. Water Marit. Energy* 106 (4): 333–344. https://doi.org/10.1680/iwtme.1994.27234.

Kuhn, M. R., and C. S. Chang. 2006. "Stability, bifurcation, and softening in discrete systems: A conceptual approach for granular materials." *Int. J. Solids Struct.* 43 (20): 6026–6051. https://doi.org/10.1016/j.ijsolstr.2005.10.012.

Meijer, L. J., T. van Emmerik, R. van der Ent, C. Schmidt, and L. Lebreton. 2021. "More than 1000 rivers account for 80% of global riverine plastic emissions into the ocean." *Sci. Adv.* 7 (18): eaaz5803. https://doi.org/10.1126/sciadv.aaz5803.

Nezu, I. 2005. "Open-channel flow turbulence and its research prospect in the 21st century." *J. Hydraul. Eng.* 131 (4): 229–246. https://doi.org/10.1061/(ASCE)0733-9429(2005)131:4(229).

Nieuwstadt, F., J. Westerweel, and B. Boersma. 2016. *Introduction to theory and applications of turbulent flows*. Cham, Switzerland: Springer.

Parthasarathy, R., and M. Muste. 1994. "Velocity measurements in asymmetric turbulent channel flows." *J. Hydraul. Eng.* 120 (9): 1000–1020. https://doi.org/10.1061/(ASCE)0733-9429(1994)120:9(1000).

Peters, M., K. Dow, S. P. Clark, J. Malenchak, and D. Danielson. 2017. "Experimental investigation of the flow characteristics beneath partial ice covers." *Cold Reg. Sci. Technol.* 142 (Oct): 69–78. https://doi.org/10.1016/j.coldregions.2017.07.007.

Piton, G., A. R. Ceron-Mayo, and S. Lambert. 2023. "Small-scale modeling of flexible barriers. II: Interactions with large wood." *J. Hydraul. Eng.* 149 (3): 04022044. https://doi.org/10.1061/JHEND8.HYENG-13071.

Rathakrishnan, E. 2007. *Instrumentation, measurements, and experiments in fluids*. Boca Raton, FL: CRC Press.

Ronckers, D., D. W. Poppema, and D. Wüthrich. 2024. "Experimental study on driftwood accumulation at submerged culverts." In *Proc., 10th Int. Symp. on Hydraulic Structures (ISHS 2024)*, 781–790. Zurich, Switzerland: ETH Zurich.

Schalko, I., C. Lageder, L. Schmocker, V. Weitbrecht, and R. M. Boes. 2019. "Laboratory flume experiments on the formation of spanwise large wood accumulations: I. Effect on backwater rise." *Water Resour. Res.* 55 (6): 4854–4870. https://doi.org/10.1029/2018WR024649.

Tatinclaux, J.-C., and M. Gogus. 1983. "Asymmetric plane flow with application to ice jams." *J. Hydraul. Eng.* 109 (11): 1540–1554. https://doi.org/10.1061/(ASCE)0733-9429(1983)109:11(1540).

Tordesillas, A., and M. Muthuswamy. 2009. "On the modeling of confined buckling of force chains." *J. Mech. Phys. Solids* 57 (4): 706–727. https://doi.org/10.1016/j.jmps.2009.01.005.

White, F. M., and J. Majdalani. 2021. *Viscous fluid flow*. New York: McGraw-Hill.

Winkelmann, J., A. Mughal, D. Weaire, and S. Hutzler. 2019. "Equilibrium configurations of hard spheres in a cylindrical harmonic potential." *Europhys. Lett.* 127 (4): 44002. https://doi.org/10.1209/0295-5075/127/44002.

Zhang, W., I. Nistor, and C. D. Rennie. 2024. "Influence of debris jam formed by trees on bridge pier scour." *J. Hydraul. Eng.* 150 (5): 04024035. https://doi.org/10.1061/JHEND8.HYENG-13688.